



# Geophysical Research Letters

## RESEARCH LETTER

10.1002/2015GL063794

### Key Points:

- Focal mechanism of tectonic tremors first determined in Taiwan
- Strong tidal modulation consistent with the focal mechanism
- Low-angle thrust mechanism suggests slip on the plate interface

### Correspondence to:

S. Ide,  
ide@eps.s.u-tokyo.ac.jp

### Citation:

Ide, S., S. Yabe, H.-J. Tai, and K. H. Chen (2015), Thrust-type focal mechanisms of tectonic tremors in Taiwan: Evidence of subduction, *Geophys. Res. Lett.*, *42*, 3248–3256, doi:10.1002/2015GL063794.

Received 10 MAR 2015

Accepted 6 APR 2015

Accepted article online 9 APR 2015

Published online 7 MAY 2015

## Thrust-type focal mechanisms of tectonic tremors in Taiwan: Evidence of subduction

Satoshi Ide<sup>1</sup>, Suguru Yabe<sup>1</sup>, Hsin-Ju Tai<sup>2</sup>, and Kate Huihsuan Chen<sup>2</sup>
<sup>1</sup>Department of Earth and Planetary Science, University of Tokyo, Tokyo, Japan, <sup>2</sup>Department of Earth Sciences, National Taiwan Normal University, Taipei, Taiwan

**Abstract** Unlike tectonic tremors in subduction zones and along transform faults, the hosting structure for tremors in Taiwan remains debated. Tectonic tremors in Taiwan have been discovered at ~30 km depth beneath the southern Central Range, which is a young and active collisional mountain belt. Here we provide the first evidence for the focal mechanism of tremor using moment tensor inversion in the very low frequency band, employing broadband seismograms stacked relative to the hypocentral time of tremor. The best solution corresponds to low-angle thrust faulting, suggesting the subduction of the Eurasian plate. This mechanism is consistent with strong tidal modulation of tremor activity but differs from the normal-type faulting that dominates regional shallow earthquakes. This result suggests vertical variations in the tectonic stress regime. Thrust faulting may be facilitated by a decrease in normal stress due to the buoyant roots of the mountain belt and local high fluid pressure.

### 1. Introduction

As a result of arc-continent collision between the Eurasian plate (EP) and the Philippine Sea plate (PSP), the mountain belt in the Central Range of Taiwan is characterized by high rates of tectonic uplift, erosion, and exhumation [e.g., Willett *et al.*, 1993, 2003; Ching *et al.*, 2011]. Beneath the southern part of the Central Range, the movement of the subducted EP shows a change from east dipping subduction to near-horizontal detachment due to the flipping of subduction polarity in Taiwan [e.g., Teng *et al.*, 2000]. In this transitional region, triggered and ambient tremors have been discovered below the seismogenic zone [Peng and Chao, 2008; Tang *et al.*, 2010; Chao *et al.*, 2012; Chuang *et al.*, 2014]. Peng and Chao [2008] discovered nonvolcanic (tectonic) tremors triggered by the surface waves of the 2001 Kunlun earthquake, while Tang *et al.* [2010] and Chao *et al.* [2012] added several examples of tremors triggered by distant earthquakes. Chuang *et al.* [2014] reported ambient tremor activity that correlates with stress change from earthquake swarms at shallow depths. In these studies, tremor distribution was restricted to a small area in the southern Central Range (Figure 1), and their deformation mechanism remains unresolved due to the limited location accuracy. Using triggered tremors, Tang *et al.* [2010] suggested that tremors occur on the deep extension of the near-vertical Chaochou-Lishan Fault, while Chao *et al.* [2012] suggested left-lateral slip on a low-angle thrust fault. Given the large errors in hypocentral locations, especially in the vertical direction, it is important to obtain direct evidence of underground movement by determining the focal mechanisms of tremors.

The determination of tremor focal mechanisms is not straightforward because signal-to-noise ratios are extremely low. Ide *et al.* [2007] obtained focal mechanisms for tremors using stacked waveforms of low-frequency earthquakes (LFEs) [Shelly *et al.*, 2006]. Similar techniques have been used in the Cascadia subduction zone [Royer and Bostock, 2014] and the Mexican subduction zone [Frank *et al.*, 2013] to obtain the focal mechanism of LFEs. In this study, we do not attempt to distinguish LFE from tremor, given that LFEs are regarded as part of successive tremors [Shelly *et al.*, 2007a]. Another way to constrain tremor focal mechanisms is to analyze very low frequency (VLF) signals observed in the 0.02–0.05 Hz range. Ide *et al.* [2008] reported that tremor signals often accompany VLF signals and that the seismic energy of tremor is always proportional to the moment rate measured in the VLF band. If this relation is universal, as suggested by a stochastic model [Ide, 2008], then the focal mechanism of VLF signals would be similar to that of tremors. The focal mechanism of some VLF signals can be determined using broadband seismograms without stacking [Ito *et al.*, 2007]. Moreover, stacking of waveforms provides a better constraint on the focal mechanism, even to lower frequencies. As demonstrated by Takeo *et al.* [2010], the

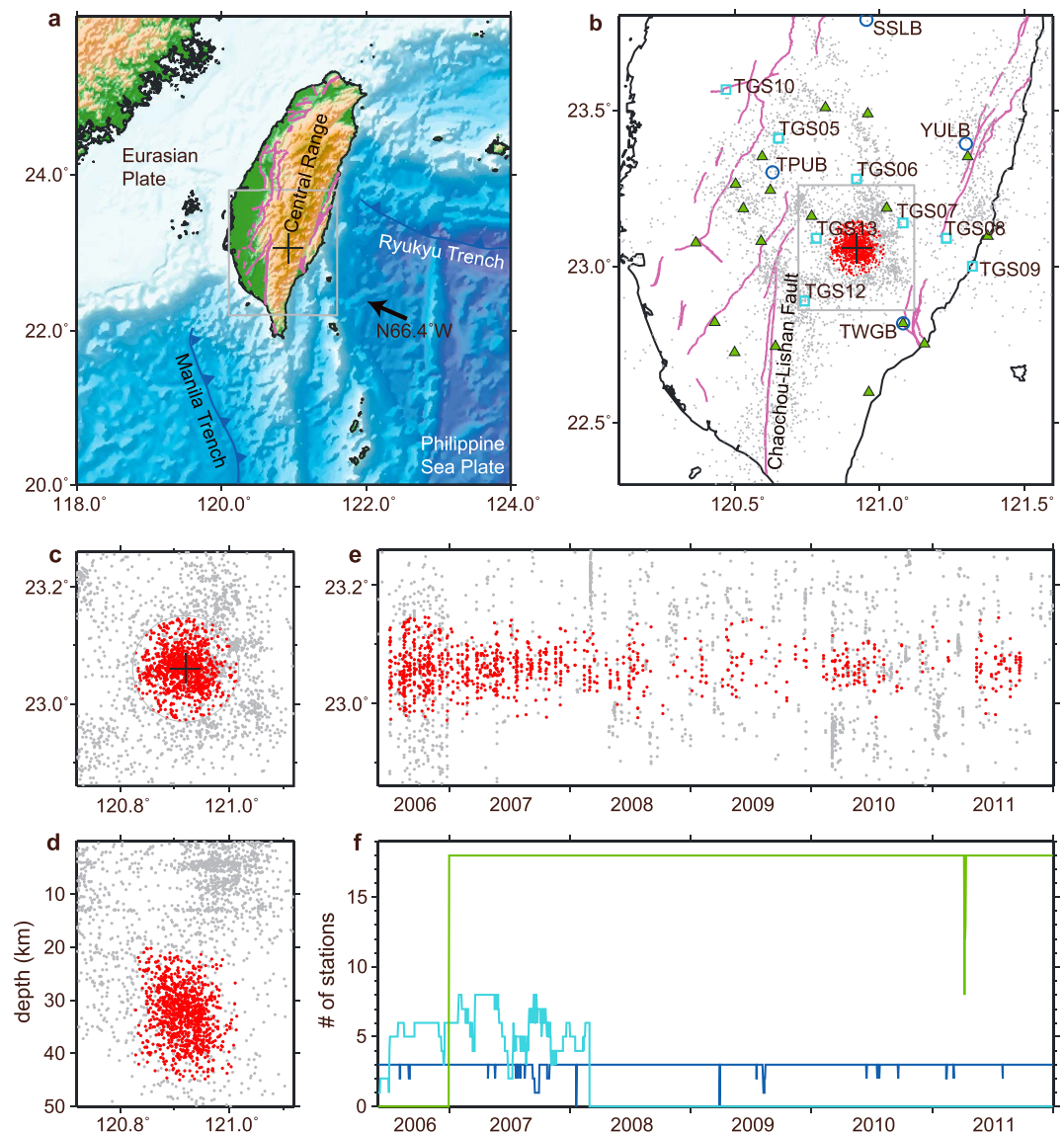


**Figure 1.** Taiwan station distribution, tremor distribution, and hypocenters. (a) Study area. Purple lines are active faults. Vector shows the plate motion of the PHP relative to the EP [Argus *et al.*, 2010]. Cross is the reference point. (b) Enlargement of the grey rectangle in Figure 1a, showing the distributions of stations and tremors. Green triangles, turquoise squares, and blue circles show CWBSN, TAIGER, and BATS stations, respectively. Grey dots are detected events, including tremors, ordinary earthquakes, and errors (false detections). Tremors used for further analyses are shown by red dots. (c) Enlargement of the grey rectangle in Figure 1b. Events within the grey circle (10 km radius) are considered tremors. (d) East-west cross section of the events in Figure 1c. (e) Space-time plot of the events in Figure 1c. (f) Station availability as a function of time. Green, turquoise, and blue lines show CWBSN, TAIGER, and BATS stations, respectively.

signals can be recovered in the 0.01–0.02 Hz range by stacking broadband signals relative to the peak of tremor amplitude. In western Japan, focal mechanisms were successfully determined from stacked waveforms in the VLF band in every 10 km radius region where sufficient tremors were observed [Ide and Yabe, 2014]. This paper applies the same stacking and inversion method to tremors in Taiwan.

Tremor focal mechanisms can also be constrained from the relation between tremors and tidal stress. Tremor activity is known to be sensitive to tidal stress [e.g., Shelly *et al.*, 2007b; Nakata *et al.*, 2008; Rubinstein *et al.*, 2008; Thomas *et al.*, 2009; Royer *et al.*, 2015], and this sensitivity varies spatially [Ide, 2010, 2012; Thomas *et al.*, 2012]. In extreme cases, such as tremors observed in Okayama prefecture in western Japan [Ide and Tanaka, 2014], tremors occur only when tidal shear stress is positive in the slip direction. Since the amplitude and phase of

shear stress change with the orientation of fault slip, for such extreme cases we can constrain possible fault plane solutions for shear motion from the timing of cataloged tremors.

## 2. Seismic Records

Three types of seismic data are used in this study, subjected to two analysis steps: construction of a tremor catalog and determination of focal mechanisms by moment tensor inversion. Short-period seismograms from the Central Weather Bureau Seismic Network (CWBSN) from January 2007 to December 2011 are used only to construct a catalog of ambient tremors. Broadband seismograms from BATS (Broadband Array in Taiwan for Seismology) for the period June 2006 to December 2011 are used for both steps. Temporary broadband seismometers installed by the TAIGER (TAiwan Integrated GEodynamics Research) project [Kuo-Chen *et al.*, 2012] from June 2006 to March 2008 are also used for both steps. The temporally changing availability of data during the study period controls the detectability of tremors, as summarized in Figure 1.

## 3. Tremor Catalog

Based on the location of ambient tremors in previous studies [Chuang *et al.*, 2014; Idehara *et al.*, 2014], we selected 28 stations from the CWBSN, TAIGER, and BATS networks located close to the center of the tremor cluster (Figure 1). Tremors were detected and located using an envelope correlation method [Obara, 2002; Ide, 2010, 2012]. All seismograms were band-pass filtered from 2 to 8 Hz, squared, low-pass filtered below 0.2 Hz, and resampled at one sample per second. Only horizontal components were used, assuming that tremor signals consist of S waves. Using waveform cross correlations between stations, we searched for tremor events in each half-overlapping time windows of 100 s. A tremor event was detected when the cross correlation exceeded 0.5 for  $\geq 10$  station pairs.

We then located the detected tremor events by solving a nonlinear inverse problem that minimize the square of misfits between observed and calculated time differences between station pairs. Theoretical travel times were calculated from the 1-D global velocity model AK135 [Kennett *et al.*, 1995], with the upper 35 km being replaced by the regional velocity model of Tang *et al.* [2010]. When the estimation error (i.e., the standard deviation of misfits between observed and calculated time differences) was larger than 2.0 s, we discarded the result. We then stacked all envelope records, time shifted by the theoretical travel times, and determined the hypocentral time of each tremor from the time of the maximum in the stacked envelope. For further details of the method, see Ide [2012]. In addition to the method employed in the previous studies, we applied a spatiotemporal clustering technique to remove isolated events, defined here as events that are separated from all other events by  $>10$  km in space or  $>1$  day in time. Most of these outliers are ordinary earthquakes or false positive detections.

Figure 1 shows the spatial and temporal distributions of tremors detected in the southern Central Range. We ascribe the temporal variation in tremor detections to changes in station availability. Although Figure 1 contains some events that are unlikely to be tremors, almost all of the events in the cluster near the cross in Figure 1 can be considered tremors. As shown in Figures 1c and 1d, the large uncertainty in hypocenter location ( $\sim 2$  km in the horizontal direction,  $\sim 5$  km in the vertical direction) means that the vertical elongation of this tremor cluster is poorly constrained.

## 4. Moment Tensor Solution in the VLF Band

We applied moment tensor inversion using four stations (SSLB, TPUB, TWGB, and YULB) from the BATS network and eight stations (TGS05, TGS06, TGS07, TGS08, TGS09, TGS10, TGS12, and TGS13) from the TAIGER network. Since five out of eight TAIGER stations have large horizontal noise, we used only vertical component data for these stations. Thus, 26 components are available. Broadband seismograms  $u_{ij}(t)$  for station  $j$  and event  $i$  are stacked relative to the hypocentral time of tremor,

$$u_j^s(t) = \frac{\sum_i u_{ij}(t)/A_i}{\sum_i 1/A_i}. \quad (1)$$

$A_i$  is the amplitude of the waveform determined in the frequency domain during an outlier control scheme, as described by Ide and Yabe [2014]. We used 942 events having epicenters within 10 km of the reference point 23.06°N, 120.92°E, and depths of 20–45 km.

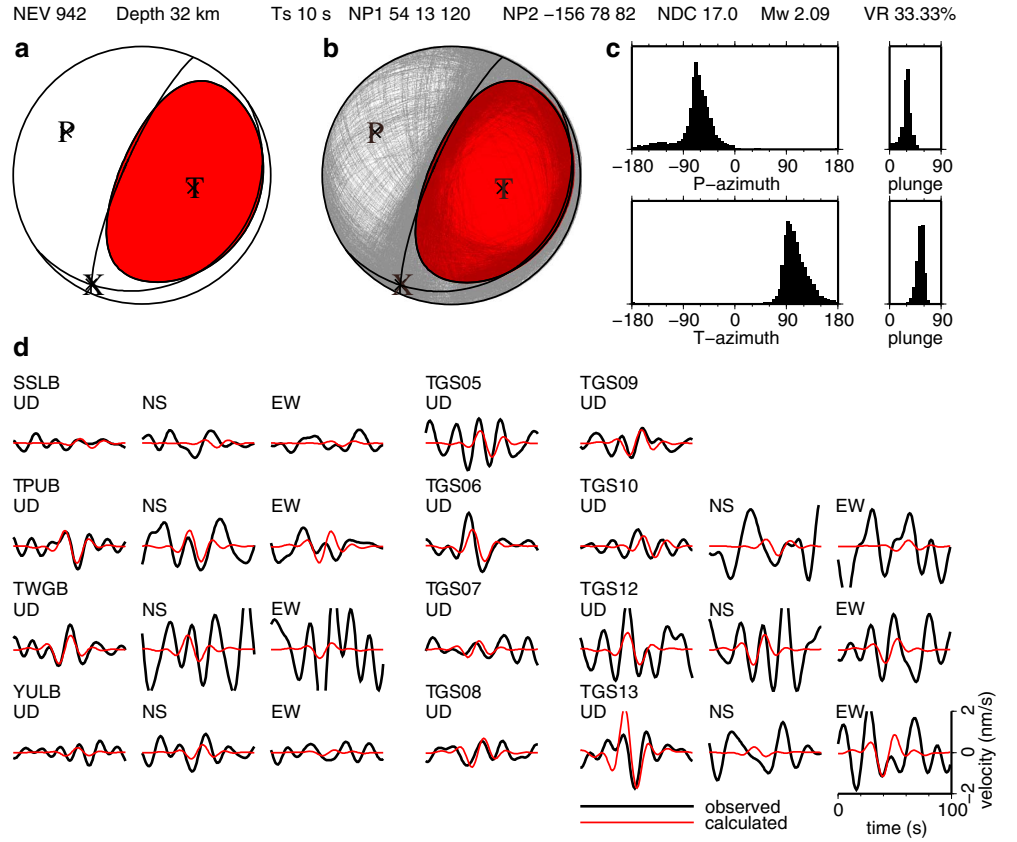


**Figure 2.** Summary of the moment tensor inversion. (a) Lower hemisphere projection (beachball diagram) for the focal mechanism. Nodal planes of the best double-couple solution and  $P$ ,  $T$ , and  $X$  axes. (b) Nodal planes of the best double-couple solutions of 1000 focal mechanisms obtained by bootstrap simulations (see text). (c) Distribution of the azimuth and plunge of  $P$  and  $T$  axes in the bootstrap simulation. (d) Comparison between observed and calculated seismic waves.

We determined a deviatoric moment tensor with five basis components  $M_i (i = 1, \dots, 5)$  by solving the linear inverse problem constructed using an observation equation

$$u_j^s(t) = \sum_i g_{ji}(t) M_i + e_j(t) / W_j, \quad (2)$$

where  $g_{ji}(t)$  is a theoretical waveform from a unit source of the  $i$ th moment tensor located at the grid point and  $D$  is the depth in kilometers. The parameter  $e_j(t)$  is the error with a standard Gaussian distribution function, and  $W_j$  is a weighting factor computed from the inverse of the maximum amplitude for 400 s before the hypocentral time. The source-time function is an isosceles triangle with a duration of  $T$  seconds. The theoretical waveform was calculated using the code of Takeo [1985], assuming the same 1-D velocity structure as used for the hypocenter determination. Both the data and calculated waves were band-pass filtered within the VLF band. The time window for analysis was extended from 30 s before to 70 s after the hypocentral time. The best fit solution was obtained by maximizing the variance reduction,

$$VR = 1 - S(\mathbf{M}) / S(0) \quad (3)$$

$$S(\mathbf{M}) = \left\| W_j u_j^s(t) - \sum_i g_{ji}(t) M_i \right\|^2, \quad (4)$$

as a function of depth  $D$  and source duration  $T$  at intervals of 1 km and 1 s, respectively.

Figure 2 shows the results of this analysis. The best estimate is obtained at  $T = 10$  s and  $D = 32$  km. The depth inferred from moment tensor inversion is close to the mean of the hypocentral depth for 942 tremors (32.5 km). Because of the band-pass filter used in the inversion, the resolution for  $T$  is not high and we obtain almost the same VR from 2 s to 12 s. Although 17% of the non-double-couple component is

included, the focal mechanism is approximately a double couple consistent with two types of fault motion: a low-angle thrust fault dipping to the east or southeast (NP1: strike  $54^\circ$ , dip  $13^\circ$ , and rake  $120^\circ$ ) and a high-angle thrust with a south southwest strike (NP2: strike  $-156^\circ$ , dip  $78^\circ$ , and rake  $82^\circ$ ). The comparison between observed and calculated waves shows generally good agreement in each vertical component, though horizontal components are not well explained due to large noise (Figure 2d).

A VR of 33% is not large compared with the results of similar studies of western Japan [Ide and Yabe, 2014]. To assess the reliability of the solution, we applied the following bootstrap method: we selected 26 seismograms, allowing duplicates of the same trace to be selected, and repeated the inversion 10,000 times. The distributions of focal planes (Figure 2b), azimuthal histograms, and  $P$  and  $T$  axes (Figure 2c) show that most solutions fall within  $30^\circ$  of the best estimate for azimuth and within  $10^\circ$  of the best estimate for plunge (Figure 2a).

## 5. Tidal Modulation and Focal Mechanism

We also found that tremors in Taiwan were strongly modulated by tidal stress. Figure 3 shows the hypocentral times of 942 tremors compared with tidal stress, which is either shear stress or normal stress acting on either NP1 or NP2 in the direction of slip (Figure 2a) at the reference point of 30 km depth. Note that it is not necessary to distinguish two planes for shear stress. The sum of the ocean and solid Earth tidal stresses is calculated using a code developed by Yabe *et al.* [2014], which employs the SPOTL software [Agnew, 2012] to calculate the ocean height with the global tide model TPXO 7.2 Atlas [Egbert and Erofeeva, 2002], the elastic Green's function of Okubo and Tsuji [2001] with a PREM structure [Dziewonski and Anderson, 1981], and the tide-generating potential of Tamura [1987] to calculate the solid Earth tide.

Figures 3a–3c show that tremors occur when tidal shear stress is positive and normal stress is negative (clamping), as indicated by the location of red dots. At this tremor location, the normal and shear stress are almost always anticorrelated. Since the clamping of normal stress suppresses slip, the increase in shear stress must be related to tremor occurrence. The amplitude of normal stress on NP2 is higher than that on NP1 by about 1 order of magnitude. Although shear slip is not impossible under high clamping stress if the friction coefficient is very small, large normal stresses acting on NP2 suggest that this plane is less likely to be the fault plane.

Figures 3d–3f compare histograms of hourly tide levels (grey) with tremor occurrence (red). Dividing the red bin by the grey bin in Figures 3d–3f, we obtain the relationship between tidal stress and tremor rate (Figures 3g–3i). Tremor rate increases nonlinearly with increasing shear stress. This relation must reflect the friction law acting in the tremor source region. Assuming an inhomogeneous Poisson process in which the tremor rate  $\lambda(t)$  is a function of shear stress  $\tau(t)$  as

$$\lambda(t) = C \exp(a\tau(t)), \quad (5)$$

we can determine the controlling parameters  $a$  and  $C$  using a maximum likelihood method (Appendix A). The maximum likelihood estimates are determined for the shear stress,  $a = 2.10 \pm 0.05 \text{ kPa}^{-1}$  and  $C = 0.0109 \pm 0.0009 \text{ h}^{-1}$  with a 95% confidence interval. The value of  $a$  is extremely large compared with estimates for Nankai and Cascadia [Yabe *et al.*, 2014], both of which are below  $1 \text{ kPa}^{-1}$ .

The relationship between tremor generation rate and shear stress depends on the focal mechanism used to calculate stress. In fact, the focal mechanism in Figure 2a is not the only mechanism that explains strong tidal modulation. In Figure 3, 94.0% of events occur when shear stress is positive. However, other mechanisms can increase the fraction of tremors with positive shear stress by up to 96.6%. To investigate this possibility, we calculated the tidal stress for 10,000 mechanisms, assuming a random distribution of  $P$  and  $T$  axes on a focal sphere. We then counted the number of tremors with positive shear stress. Figure 4 shows the directions of  $P$  and  $T$  axes that explain large fractions of tremors with positive shear stress. Generally, tidal sensitivity appears large for a combination of a near-vertical  $T$  axis and a near-horizontal  $P$  axis in the east-northeast direction. Since a near-vertical  $T$  axis is necessary to explain the observed strong tidal correlation, we can exclude some focal mechanisms from the candidates: for example, a strike-slip fault with nearly horizontal  $P$  and  $T$  axes does not satisfy this condition. A left-lateral slip on a low-angle fault, as proposed by Chao *et al.* [2012], is also unlikely.

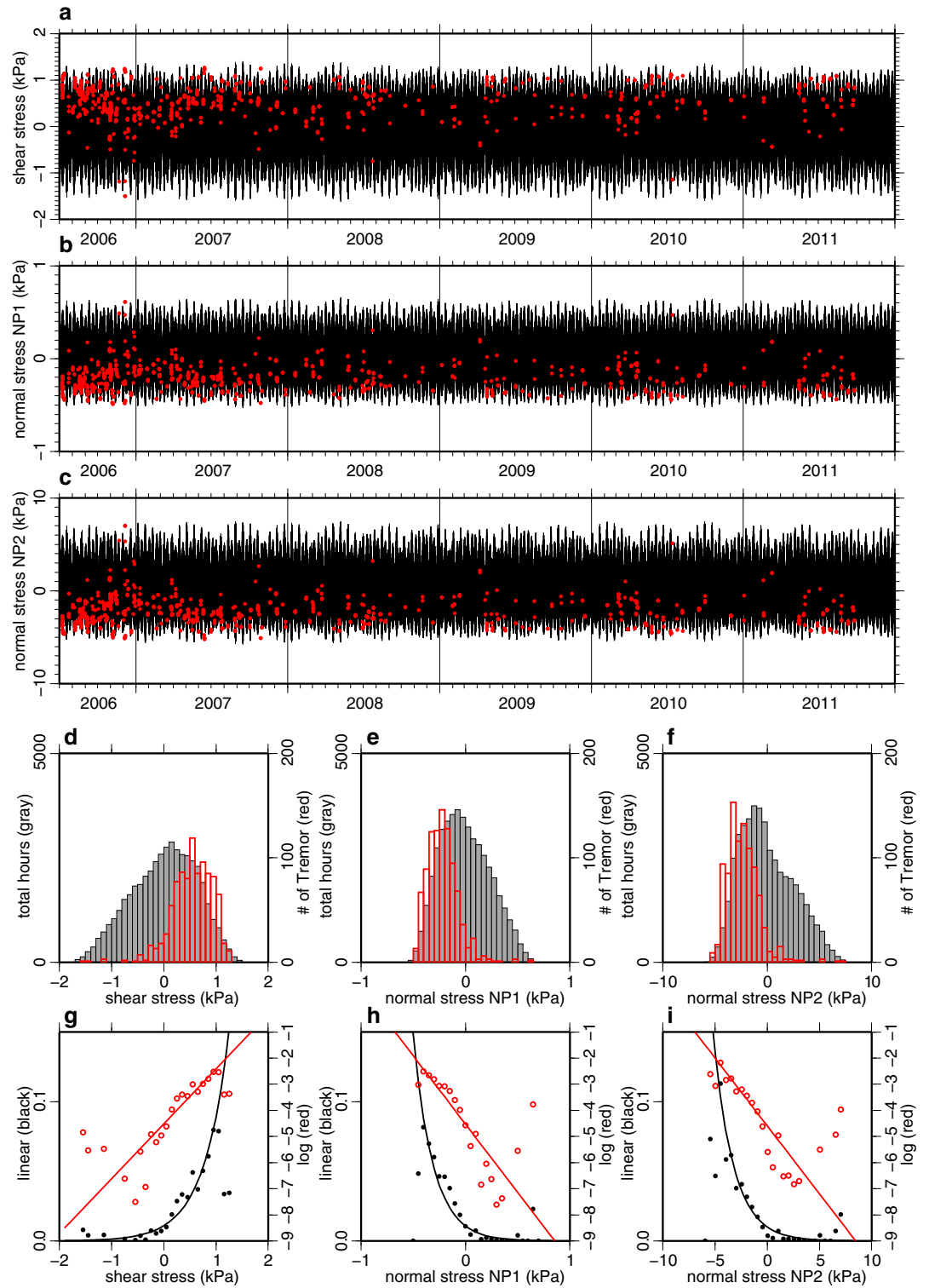


**Figure 3.** Tremor activity and tidal stress. (a) Tidal shear stress calculated for NP1 and NP2. Red dots are plotted at the timing of tremors. (b) Same as Figure 3a but for normal stress on NP1. (c) Same as Figure 3a but for normal stress on NP2. (d) Histogram of hourly levels of shear stress (grey) and the number of tremors (red) for the study period. (e) Same as Figure 3d but for normal stress on NP1. (f) Same as Figure 3d but for normal stress on NP2. (g) Number of tremors per hour for each bin in linear (black) and semilog plots (red) for shear stress. The lines calculated using MLE estimates of two parameters are also shown. (h) Same as Figure 3g but for normal stress on NP1. (i) Same as Figure 3g but for normal stress on NP2.

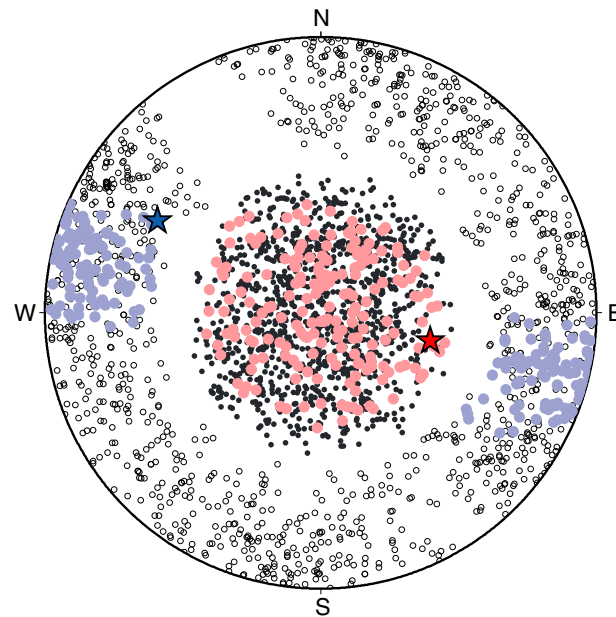


**Figure 4.** Distribution of  $P$  and  $T$  axes consistent with strong tidal modulation of tremor. Open and solid circles indicate the locations of  $P$  and  $T$  axes, respectively, of focal mechanisms for which  $>94.0\%$  of events occur with positive shear stress. Light blue and pink circles indicate cases for which  $>96.6\%$  of events occur with positive shear stress. Blue and red stars are the  $P$  and  $T$  axes of the solution in Figure 2.

## 6. Discussion and Conclusions

Unlike worldwide subduction zones and major fault systems, the structure that hosts tremors in Taiwan is controversial. The southern Central Range is the transition region between subduction of EP underneath PSP and collision with the Luzon arc, and the underlying structure in this region remains poorly resolved. *Peng and Chao* [2008] proposed a sub-horizontal décollement at 10 km depth based on triggered tremor locations and the correlation between triggered tremor timing and Love-wave-induced stress. Using the location of LFEs, *Tang et al.* [2010] inferred that a high-angle thrust with a strike-slip component is more plausible. This is consistent with the Chaochou-Lishan Fault. In discussing the stress-triggering relation between ambient tremor and shallow earthquake activity, *Chuang et al.* [2014] considered two possibilities: a thrust fault plane aligned along a décollement, following the wedge model of *Carena et al.* [2002], and a vertically oriented normal fault plane that is similar to swarm focal mechanisms.

In this study, tremor locations are concentrated at depths of 25–40 km (mean 32.5 km), much deeper than the proposed décollement at 10 km. We show the first evidence of subsurface structure in this depth range by determining the tremor focal mechanism. Our result shows either low-angle thrust slip (NP1) or high-angle thrust slip (NP2) as a possible deformation mechanism around the tremor source. Assuming this mechanism, we can clearly show that tremors occur primarily when tidal shear stress is high. Since tidal normal stress acts against the slip in this region, the large amplitude of NP2 is unlikely. Thus, the evidence favors thrust slip on a low-angle fault dipping to the east or southeast as the most likely mechanism for tremor activity.

As proposed by *Chuang et al.* [2014], ambient tremor location is consistent with areas of high geothermal gradient, high uplift rate, low  $Q_p$ , an electromagnetic conductivity boundary, and abundant normal faulting in the upper crust. These lines of geophysical evidence, combined with the special tectonic setting of the study region, indicate that the detachment of the EP is a result of the flipping of subduction polarity in Taiwan and was initiated from the east dipping Eurasian slab in the south. Therefore, this region has experienced enough subduction to produce metamorphic fluids and enough extension to accelerate their release.

In the upper crust, from near surface to 15 km depth, earthquakes appear to show normal faulting mechanisms with NE-SW striking  $T$  axes. The minimum compressive stress runs subparallel to the strike of the Taiwan orogeny [*Rau and Wu*, 1998; *Rau et al.*, 2011]. The deeper tremors, however, reveal a vertical  $T$  axis rather than horizontal, indicating a different mechanism to that of shallow earthquakes. Together with the nearly E-W striking  $P$  axis, we propose that along with the transition from subduction to collision, the extrusion of hot buoyant Chinese continental basement could occur in the tremor source region.

The faulting mechanism of tremors at ~30 km is unlikely to be associated with slip on the shallow décollement (~10 km). Instead, because the southern Central Range is characterized by a deep thermal anomaly, the mountain's buoyant roots [e.g., *Kuo-Chen et al.*, 2012] act to decrease normal stress. This could facilitate thrust faulting in the deeper crust and the subduction of the EP. A large amount of fluid and low vertical stress may explain the observed sensitivity of tremors to small tidal stresses, despite the high confining stress at depth.

## Appendix A

Assume that tremor occurrence is governed by an inhomogeneous Poisson process, in which the rate parameter  $\lambda(t)$  changes according to equation (5). For a sufficiently small time interval  $\Delta t$ , the probability that an event occurs,  $P(1)$ , and does not occur,  $P(0)$ , can be respectively written as

$$P(1) = \lambda(t)\Delta t \exp(-\lambda(t)\Delta t), \quad (A1)$$

$$P(0) = \exp(-\lambda(t)\Delta t). \quad (A2)$$

For  $N$  tremors occurring at  $i_1 = 1, i_2, i_3, \dots$ , and  $i_N = M$  of  $M(\gg N)$  successive time windows of  $\Delta t$ , the joint probability of occurrence is

$$\prod_{k=1}^N \lambda(i_k \Delta t) \Delta t \times \exp \sum_{k=1}^M -\lambda(k \Delta t) \Delta t. \quad (A3)$$

Substituting equation (5), we obtain a likelihood function for two parameters  $a$  and  $C$ ,

$$L(a, C) = \prod_{k=1}^N C \exp(a\tau(t_k)) \Delta t \times \exp \sum_{k=1}^M -C \exp(a\tau(k \Delta t)) \Delta t. \quad (A4)$$

The corresponding log likelihood function is

$$\log L(a, C) = N \log C + \sum_{k=1}^N a\tau(t_k) - \sum_{k=1}^M C \exp(a\tau(k \Delta t)) \Delta t + \text{const.} \quad (A5)$$

The maximum of this function is obtained at

$$C = N / \sum_{k=1}^M \exp(a\tau(k \Delta t)) \Delta t. \quad (A6)$$

The maximum likelihood estimate of  $a$  is obtained numerically by searching the maximum of the function (A5).

## Acknowledgments

This work is supported by JSPS KAKENHI (23244090) and by Taiwan MOST grant MOST 103-2116-M-003-001-MY5. GMT software [Wessel and Smith, 1991] was used to draw figures. The data for this paper are available at the data server of Incorporated Research Institutions for Seismology for TAIGER and BATS, and from Geophysical Database Management System (GDMS) by Central Weather Bureau in Taiwan. We are grateful to Timothy Byrne for the helpful discussion in tectonic interpretation. We also thank Amanda Thomas and an anonymous reviewer for helpful comments.

The Editor thanks Amanda Thomas and one anonymous reviewer for their assistance in evaluating this paper.

## References

- Agnew, D. C. (2012), SPOTL: Some programs for ocean-tide loading, SIO Tech. Rep., Scripps Institution of Oceanography.
- Argus, D. F., R. G. Gordon, M. B. Heflin, C. Ma, R. J. Eanes, P. Willis, W. R. Peltier, and S. E. Owen (2010), The angular velocities of the plates and the velocity of Earth's centre from space geodesy, *Geophys. J. Int.*, **180**, 913–960.
- Carena, S., J. Suppe, and H. Kao (2002), Active detachment of Taiwan illuminated by small earthquakes and its control of first-order topography, *Geology*, **30**(10), 935–938.
- Chao, K., Z. Peng, C. Wu, C.-C. Tang, and C.-H. Lin (2012), Remote triggering of non-volcanic tremor around Taiwan, *Geophys. J. Int.*, **188**, 301–324, doi:10.1111/j.1365-246X.2011.05261.x.
- Ching, K. E., R. J. Rau, K. M. Johnson, J. C. Lee, and J. C. Hu (2011), Present-day kinematics of active mountain building in Taiwan from GPS observations during 1995–2005, *J. Geophys. Res.*, **116**, doi:10.1029/2010JB008058.
- Chuang, L. Y., K. H. Chen, A. Wech, T. Byrne, and W. Peng (2014), Ambient tremors in a collisional orogenic belt, *Geophys. Res. Lett.*, **41**, 1485–1491, doi:10.1002/2014GL059476.
- Dziewonski, A. M., and A. Anderson (1981), Preliminary reference Earth model, *Phys. Earth Planet. Inter.*, **25**, 297–356.
- Egbert, G. D., and L. Erofeeva (2002), Efficient inverse modeling of barotropic ocean tides, *J. Atmos. Oceanic Technol.*, **19**, 183–204.
- Frank, W. B., N. M. Shapiro, V. Kostoglodov, A. L. Husker, M. Campillo, J. S. Payero, and G. A. Prieto (2013), Low-frequency earthquakes in the Mexican Sweet Spot, *Geophys. Res. Lett.*, **40**, 2661–2666, doi:10.1002/grl.120561.
- Ide, S. (2008), A Brownian walk model for slow earthquakes, *Geophys. Res. Lett.*, **35**, L17301, doi:10.1029/2008GL034821.
- Ide, S. (2010), Striations, duration, migration and tidal response in deep tremor, *Nature*, **466**, 356–359, doi:10.1038/nature09251.
- Ide, S. (2012), Variety and spatial heterogeneity of tectonic tremor worldwide, *J. Geophys. Res.*, **117**, B03302, doi:10.1029/2011JB008840.
- Ide, S., and Y. Tanaka (2014), Controls on plate motion by oscillating tidal stress: Evidence from deep tremors in western Japan, *Geophys. Res. Lett.*, **41**, 3842–3850, doi:10.1002/2014GL060035.
- Ide, S., and S. Yabe (2014), Universality of slow earthquakes in the very low frequency band, *Geophys. Res. Lett.*, **41**, 2786–2793, doi:10.1002/2014GL059712.
- Ide, S., D. R. Shelly, and G. C. Beroza (2007), The mechanism of deep low frequency earthquakes: Further evidence that deep non-volcanic tremor is generated by shear slip on the plate interface, *Geophys. Res. Lett.*, **34**, L03308, doi:10.1029/2006GL028890.
- Ide, S., K. Imanishi, Y. Yoshida, G. C. Beroza, and D. R. Shelly (2008), Bridging the gap between seismically and geodetically detected slow earthquakes, *Geophys. Res. Lett.*, **35**, L10305, doi:10.1029/2008GL034014.
- Idehara, K., S. Yabe, and S. Ide (2014), Regional and global variations in the temporal clustering of tectonic tremor activity, *Earth Planets Space*, **66**, 1–10.
- Ito, Y., K. Obara, K. Shiomi, S. Sekine, and H. Hirose (2007), Slow earthquakes coincident with episodic tremors and slow slip events, *Science*, **315**, 503–506, doi:10.1126/science.1134454.
- Kennett, B. L. N., E. R. Engdahl, and R. Buland (1995), Constraints on seismic velocities in the Earth from travel times, *Geophys. J. Int.*, **122**, 108–124.
- Kuo-Chen, H., F. T. Wu, and S. W. Roecker (2012), Three-dimensional  $P$  velocity structures of the lithosphere beneath Taiwan from the analysis of TAIGER and related seismic data sets, *J. Geophys. Res.*, **117**, B06306, doi:10.1029/2011JB009108.

- Nakata, R., N. Suda, and H. Tsuruoka (2008), Non-volcanic tremor resulting from the combined effect of Earth tides and slow slip events, *Nat. Geosci.*, *1*, 676–678.
- Obara, K. (2002), Nonvolcanic deep tremor associated with subduction in southwest Japan, *Science*, *296*, 1679–1681.
- Okubo, S., and D. Tsuji (2001), Complex Green's function for diurnal/semidiurnal loading problems, *J. Geod. Soc. Japan*, *47*, 225–230.
- Peng, Z., and K. Chao (2008), Non-volcanic tremor beneath the Central Range in Taiwan triggered by the 2001 *Mw* 7.8 Kunlun earthquake, *Geophys. J. Int.*, *175*, 825–829.
- Rau, R., K. Ching, Y. Lee, J. Lee, Y. Chan, and T. B. Byrne (2011), Orogenic extension during arc-continent collision: Constrained by earthquake analysis in south central Taiwan, AGU Fall Meeting 2011, abstract #T52C-03.
- Rau, R. J., and F. T. Wu (1998), Active tectonics of Taiwan orogeny from focal mechanisms of small-to-moderate-sized earthquakes, *TAO*, *9*(4), 755–778.
- Royer, A. A., and M. G. Bostock (2014), A comparative study of low frequency earthquake templates in northern Cascadia, *Earth Planet. Sci. Lett.*, *402*, 247–256.
- Royer, A. A., A. M. Thomas, and M. G. Bostock (2015), Tidal modulation and triggering of low-frequency earthquakes in northern Cascadia, *J. Geophys. Res. Solid Earth*, *120*, 384–405, doi:10.1002/2014JB011430.
- Rubinstein, J. L., M. La Rocca, J. E. Vidale, K. C. Creager, and A. G. Wech (2008), Tidal modulation of nonvolcanic tremor, *Science*, *319*, 186–189, doi:10.1126/science.1150558.
- Shelly, D. R., G. C. Beroza, S. Ide, and S. Nakamura (2006), Low-frequency earthquakes in Shikoku Japan, and their relationship to episodic tremor and slip, *Nature*, *442*, 188–191, doi:10.1038/nature04931.
- Shelly, D. R., G. C. Beroza, and S. Ide (2007a), Complex evolution of transient slip derived from precise tremor locations in western Shikoku, Japan, *Geochem. Geophys. Geosyst.*, *8*, Q10014, doi:10.1029/2007GC001640.
- Shelly, D. R., G. C. Beroza, and S. Ide (2007b), Non-volcanic tremor and low-frequency earthquake swarms, *Nature*, *446*, 305–307.
- Takeo, A., et al. (2010), Very broadband analysis of a swarm of very low frequency earthquakes and tremors beneath Kii Peninsula, SW Japan, *Geophys. Res. Lett.*, *37*, L06311, doi:10.1029/2010GL042586.
- Takeo, M. (1985), Near-field synthetic seismograms taking into account the effects of anelasticity: The effects of anelastic attenuation on seismograms caused by a sedimentary layer (in Japanese), *Meteorol. Geophys.*, *36*, 245–257.
- Tamura, Y. (1987), A harmonic development of the tide-generating potential, *Bull. Inf. Marées Terrestres*, *99*, 6813–6855.
- Tang, C. C., Z. Peng, K. Chao, C. H. Chen, and C. H. Lin (2010), Detecting low-frequency earthquakes within non-volcanic tremor in southern Taiwan triggered by the 2005 *Mw* 8.6 Nias earthquake, *Geophys. Res. Lett.*, *37*, L16307, doi:10.1029/2010GL043918.
- Teng, L. S., C. T. Lee, Y. B. Tsai, and L. Y. Hsiao (2000), Slab breakoff as a mechanism for flipping of subduction polarity in Taiwan, *Geology*, *28*(2), 155–158.
- Thomas, A. M., R. M. Nadeau, and R. Bürgmann (2009), Tremor-tide correlations and near-lithostatic pore pressure on the deep San Andreas fault, *Nature*, *462*, 1048–1051, doi:10.1038/nature08654.
- Thomas, A. M., R. Bürgmann, D. R. Shelly, N. M. Beeler, and M. L. Rudolph (2012), Tidal triggering of low frequency earthquakes near Parkfield, California: Implications for fault mechanics within the brittle-ductile transition, *J. Geophys. Res.*, *117*, B05301, doi:10.1029/2011JB009036.
- Wessel, P., and W. H. Smith (1991), Free software helps map and display data, *Eos Trans. AGU*, *72*(41), 441–446, doi:10.1029/90EO00319.
- Willett, S., C. Beaumont, and P. Fullsack (1993), Mechanical model for the tectonics of doubly vergent compressional orogens, *Geology*, *21*(4), 371–374.
- Willett, S. D., D. Fisher, C. Fuller, Y. En-Chao, and L. Chia-Yu (2003), Erosion rates and orogenic-wedge kinematics in Taiwan inferred from fission-track thermochronometry, *Geology*, *31*(11), 945–948.
- Yabe, S., S. Ide, Y. Tanaka, and H. Houston (2014), Tidal stress influence on the deep plate interface, AGU fall meeting, S52B-05.